Nanoscale Advances

ROYAL SOCIETY OF CHEMISTRY

PAPER

View Article Online
View Journal | View Issue



Cite this: *Nanoscale Adv.*, 2024, **6**, 4657

# An ordered mesoporous carbon–silica hybrid for the detection of the antiviral drug ribavirin in clinical samples†

Amir Hosein Ali Naghian,[a] Zahra Hashemi,[a] Fereshteh Chekin *[b] and Na'il Saleh *[c]

Ribavirin (RIB) is widely used for the treatment of viral diseases such as herpes, hepatitis C, and Lassa fever. Moreover, to control the spread of COVID-19, the consumption of antiviral medicines, including RIB, has increased significantly worldwide. By combining ordered mesoporous carbon with silica nanoparticles *via* ultrasound, we synthesized silica/ordered mesoporous carbon ($SiO_2$–OMC) hybrid composites that show excellent electrochemical performance. The hybrid composite was found to contain spherical $SiO_2$ nanoparticles having diameters ranging from 21 to 29 nm. A sensor comprising a carbon paste electrode and $SiO_2$–OMC ($SiO_2$–OMC/CPE) facilitated the ultrasensitive and selective detection of RIB at an oxidation potential of 0.71 V, having a linear range of 0.1–40 μmol $L^{-1}$, limit of detection of 0.067 μmol $L^{-1}$, and sensitivity of 1.969 μA $\mu mol^{-1}$ L. Furthermore, the results indicate that charge transfer at the interface of the $SiO_2$–OMC hybrid results in a synergistic effect compared to OMC and $SiO_2$ alone. The advantages include the potential for regenerating the sensor surface, rapid and facile production, and suitability for the detection of RIB in capsule, human plasma, and urine samples, making $SiO_2$–OMC/CPE a promising interface for bioelectrochemical applications.

Received 25th May 2024
Accepted 15th July 2024

DOI: 10.1039/d4na00435c

rsc.li/nanoscale-advances



## Introduction

Hepatitis C virus (HCV) is the leading cause of liver disease.[1] The combination of polyethylene glycol (PEG)ylated-interferon α and ribavirin (RIB) is currently recommended for the treatment of HCV.[2] RIB ([[(2*R*,3*R*,4*S*,5*R*)-3,4-dihydroxy-5-(hydroxymethyl)oxolan-2-yl]-1,2,4-triazole-3-carboxamide) is a synthetic analogue of a purine nucleoside[3] and is a broad-spectrum antiviral agent effective against both DNA and RNA viruses. It has proven efficacious in treating HCV infections, especially when used in conjunction with interferon α-2a/2b or PEGylated-interferon α-2a/2b.[4,5] RIB is also the sole medication prescribed for Lassa fever, haemorrhagic fevers, severe acute respiratory syndrome (SARS), serious respiratory syncytial virus infections in paediatric patients, and influenza A and B viruses.[6] The mechanisms of action of RIB include modulating the imbalance between T-helper-1 and -2 lymphocytes, depleting cellular guanosine triphosphate by inhibiting inosine monophosphate dehydrogenase, obstructing viral RNA-dependent RNA polymerase, impairing translation by preventing the capping of messenger viral RNA, and inducing lethal viral mutagenesis.[7]

The COVID-19 pandemic has seen clinical development and use of antiviral therapies at an unprecedented speed. Antiviral therapies have greatly improved the clinical outcome in COVID-19 patients, especially when administered early after diagnosis.[8] However, the presence of antiviral drugs in aquatic environments has triggered alarm concerning damage to natural ecosystems and human health.[9] In particular, RIB is associated with considerable side effects; over 10% of patients experience dermatological, endocrine, metabolic issues, anorexia, nausea, vomiting, and anaemia.[10] The hazards linked with RIB and its primary metabolites include haemolysis, genetic and reproductive toxicity, and teratogenicity.[11] Hence, antiviral medications such as RIB are emerging primary pollutants.

Various analytical methods including thin-layer chromatography,[12] high-pressure liquid chromatography,[13] liquid chromatography-tandem mass spectrometry,[14] flow injection chemiluminescence,[15] capillary electrophoresis,[16] and voltammetry[17–20] have been employed to quantify RIB in clinical specimens. Electrochemical sensors such as the 3-aminophenyl boronic acid/reduced graphene oxide/glassy carbon electrode(APBA/RGO/GCE),[17] hanging mercury drop electrode (HMDE),[18] glassy carbon electrode modified with molecularly imprinted membrane/Prussian blue-gold (MIM/Au-PB/GCE),[19] and Pt electrodes[20] have been shown to be feasible tools for RIB detection.

[a]*Department of Pharmacy, Ayatollah Amoli Branch, Islamic Azad University, Amol, Iran*

[b]*Department of Chemistry, Ayatollah Amoli Branch, Islamic Azad University, Amol, Iran. E-mail: fchekin@yahoo.com; Tel: +981143217076*

[c]*Department of Chemistry, College of Science, United Arab Emirates University, Al Ain 15551, United Arab Emirates. E-mail: n.saleh@uaeu.ac.ae; Tel: +97137136138*

† Electronic supplementary information (ESI) available. See DOI: https://doi.org/10.1039/d4na00435c

Ordered mesoporous materials having diameters ranging from 2 to 50 nm have been extensively investigated for a wide range of applications, including adsorption, separation, catalysis, drug delivery, energy conversion, and storage.[21,22] Owing to their hierarchical and modifiable porous architectures, mesoporous materials are frequently utilised in catalysis, sorption, separation, and biomedicine. Recently, ordered mesoporous carbons (OMC) have garnered considerable interest because of their distinctive hexagonal structures, adjustable large pore volumes, high thermal stabilities, and substantial surface area to volume ratios.[23] Furthermore, the bimodal structure of OMCs may enhance electron and ion transfer, leading to OMC composites having high current densities. Amongst OMC materials, CMK-3 is distinguished by its ordered carbon nanowire arrays, which have a high length-to-diameter ratio.[24] Additionally, CMK-3 can be readily customised in terms of pore size and wall thickness for practical applications. The macroscopic coarse particle structure of CMK-3 also aids its dispersion within a matrix, making it a promising candidate for the fabrication of composites as catalytic materials.[25]

Electroanalytical devices based on silica have also been developed. In particular, the attractive structures of silica have driven the development of mesoporous silica-based sensors and biosensors that show enhanced performance relative to their non-ordered counterparts.[26] To the best of our knowledge, there is no prior reports in literature on the electro-catalytic behavior of $SiO_2$–OMC nanocomposite. By combining $SiO_2$ nanoparticles and OMC porous framework, an excellent nanocomposite was created with high surface area and good conductivity to improve the surface of electrodes. The prepared modified electrode demonstrated remarkable electro-catalytic activity for the detection of RIB in clinical samples with reasonable analytical results.

# Experimental

### Chemicals

OMC, sodium silicate, RIB, potassium hexacyanoferrate(II), phosphoric acid and its salts, graphite powder, and sodium hydroxide were obtained from Sigma-Aldrich. Green tea, predominantly cultivated in Rasht Province, was also used in this study. Human plasma and urine samples were prepared from clinical laboratory tests, Amol. All experiments were performed and informed consent was obtained in accordance with the Guidelines for Care and Use of Clinical Laboratory in Amol.

### Apparatus

The surface morphology and chemical composition of the samples were analysed using scanning electron microscopy (SEM; MIRATESCAN-XMU, Czech Republic) and energy dispersive X-ray spectroscopy (EDS). Ultraviolet-visible (UV-vis) spectrophotometry was carried out using a UV-1900 device (Shimadzu Co., Japan). Raman spectra were obtained on a Takram P50C0R10 Raman spectrometer (Teksan, Iran). X-ray diffractometry (XRD) measurements were performed with a Bruker D8 Advance X-ray diffractometer (Germany). Electrochemical measurements were carried out using a potentiostat/galvanostat (Sama 500-c, Sama, Iran). A platinum wire (as an auxiliary electrode), Ag|AgCl|KCl (as the reference electrode), carbon paste electrode (CPE), and $SiO_2$–OMC/CPE (as working electrodes) were employed in the electrochemical cell.

### Ultrasonic assisted extraction (UAE)

Green tea (2 g) was infused in distilled water (100 mL) and sonicated in an ultrasound bath (60 kHz) at 45 °C for 20 min. The extract was filtered using Whatman filter paper and stored at 4 °C.

### Synthesis of $SiO_2$–OMC nanocomposites

A 10 mL aliquot of the extract was combined with sodium silicate (20 mL, 0.5 M) with constant stirring at 60 °C and sonicated for 30 min. The pH of the mixture was adjusted to 9.0 using NaOH (1.0 M). The mixture was refluxed for 10 h at 50 °C, centrifuged for 10 min, washed with water, and heated at 600 °C for 1 h. The resultant product was composed of $SiO_2$ powder. OMC (10 mg) and $SiO_2$ nanoparticles (10 mg) were added to distilled water (30 mL), and the mixture was sonicated for 30 min at 25 °C. The product ($SiO_2$–OMC) was washed with water and dried at 60 °C overnight.

### Fabrication of $SiO_2$–OMC nanocomposite modified electrode

The CPE was prepared following our previously reported method.[27,28] Graphite powder and paraffin were mixed manually until a uniformly wetted paste was achieved. The carbon paste was then packed into a glass tube (internal diameter of 3 mm). Electrical contacts were established using a copper wire. Subsequently, a fresh electrode surface was exposed by polishing with paper. Then, $SiO_2$–OMC (1 mg) nanocomposite was dispersed in ethanol (1 mL) and sonicated for 30 min. Finally, the dispersion (5 μL) was drop-cast onto the CPE and dried in an oven at 50 °C.

### Analysis of biological samples

Human serum plasma or urine (500 μL) were aliquoted into phosphate buffer solution (PBS; 10 mL, 0.1 mol $L^{-1}$; pH 7.0), and electrochemical analysis was performed by cyclic voltammetry(CV). Additionally, the samples were analysed by UV-vis spectroscopy at a wavelength of 220 nm after the addition of the samples (500 μL) to PBS (5 mL, 0.1 M; pH 7.0).

# Results and discussion

### Characterisation

The morphologies of OMC, $SiO_2$, and $SiO_2$–OMC were characterised using field-emission (FE)-SEM. As shown in Fig. 1, OMC has a plate-like structure (Fig. 1A), whereas $SiO_2$ displays aggregated spherical nanoparticles (Fig. 1B). The SEM image of $SiO_2$–OMC reveals $SiO_2$ nanoparticles enveloping the OMC layers (Fig. 1C), having diameters ranging from 21 to 29 nm (Fig. 1D). The EDS spectrum of $SiO_2$–OMC (Fig. 2A) reveals that the sample comprises C (73.21%), O (18.44%), and Si (8.36%

 

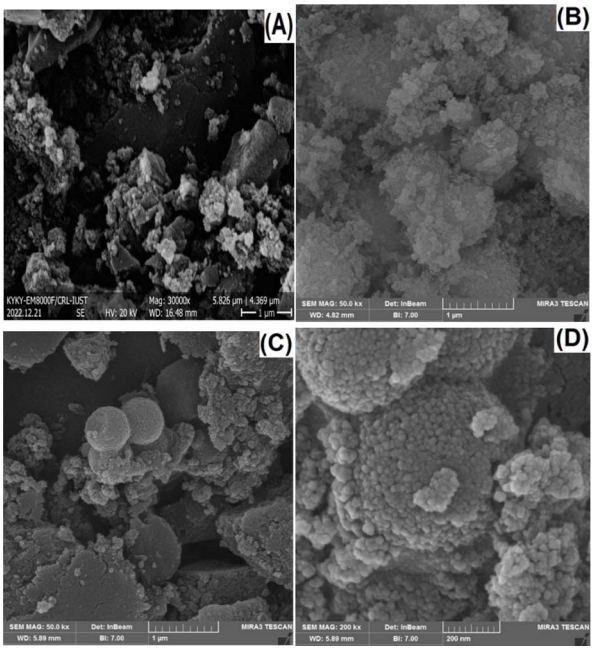


Fig. 1 FE-SEM images of OMC (A), $SiO_2$ (B) and $SiO_2$–OMC (C) and (D) at different scales.

W), confirming the synthesis of the $SiO_2$–OMC hybrid. Additionally, elemental mapping demonstrates a uniform distribution of Si in $SiO_2$–OMC (Fig. 2B).

Raman analysis was conducted on OMC, $SiO_2$, and $SiO_2$–OMC (Fig. 3A) to assess the defects introduced into the OMC structure after decoration with $SiO_2$ nanoparticles. The D and G bands of OMC appeared at 1340 and 1603 $cm^{-1}$, respectively, with an intensity ratio ($I_D/I_G$) of 0.98. $SiO_2$ did not exhibit any peaks within this range. For $SiO_2$–OMC, the D and G bands shifted to 1346 and 1598 $cm^{-1}$, respectively, and the $I_D/I_G$ ratio increased to 1.06, indicating chemical interactions between $SiO_2$ and OMC.

XRD analysis was employed to examine the crystalline structure and interlayer modifications of the samples. The XRD patterns of OMC, $SiO_2$, and $SiO_2$–OMC are shown in Fig. 3B. The characteristic peaks of OMC at 24° and 45° correspond to the

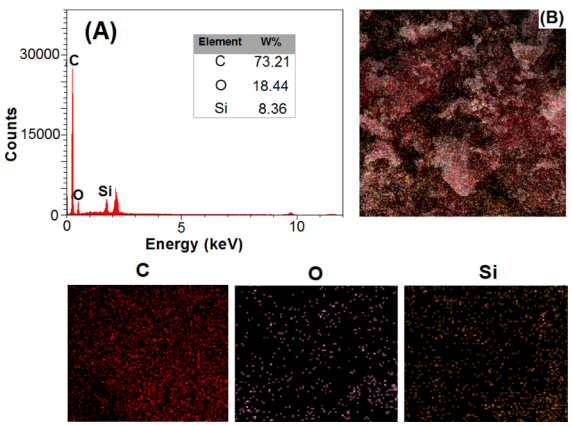


Fig. 2 EDS spectrum (A) and elemental maps (B) of $SiO_2$–OMC.

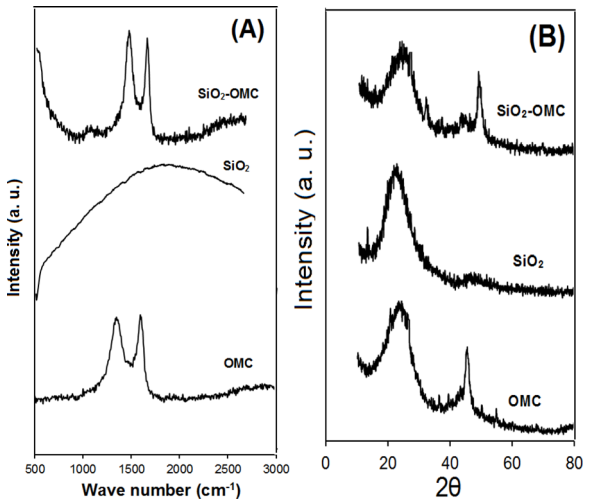


Fig. 3 Raman spectra (A) and XRD patterns (B) of OMC, $SiO_2$, and $SiO_2$–OMC.

(002) and (100) planes, respectively. The $SiO_2$ nanoparticles demonstrated a peak at 22.5°, consistent with the JCPDS89-0510 card. The (002) and (100) diffraction peaks of $SiO_2$–OMC shifted to 25° and 48°, respectively, suggesting changes owing to the incorporation of $SiO_2$ particles onto OMC.

The UV spectra of aqueous dispersions containing OMC, $SiO_2$, and $SiO_2$–OMC are presented in Fig. 4A. OMC did not show any significant absorption peak at 200–400 nm. In contrast $SiO_2$ yielded a broad absorption peak at 279 nm, which, after integration with OMC, shifted to 282 nm, indicating the formation of the $SiO_2$–OMC hybrid.

Fig. 4B illustrates the electrochemical behaviour of $[Fe(CN)_6]^{3-/4-}$ with the CPE and modified CPEs in PBS (0.1 mol $L^{-1}$, pH 7.0), as determined by CV measurements. The current of the $SiO_2$–OMC/CPE exceeded those recorded with the CPE, $SiO_2$/CPE, and OMC/CPE. OMC and $SiO_2$ nanostructures are known to have high surface areas, excellent electrical conductivities, rapid electron transfers, and current enhancement. The active surface areas of the OMC, $SiO_2$, and $SiO_2$–OMC interfaces were estimated by plotting the peak current against the square root of the scan rate,[29] yielding values of 0.07, 0.09, 0.15, and 0.19 $cm^2$ for CPE, $SiO_2$/CPE, OMC/CPE, and $SiO_2$–OMC/CPE, respectively. Benefiting from the synergistic

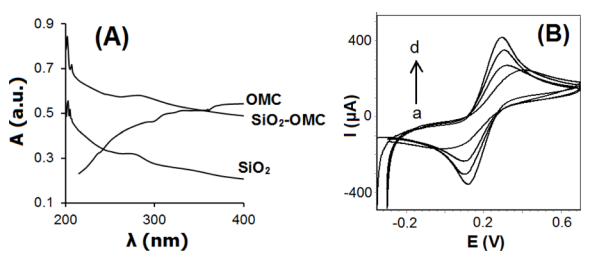


Fig. 4 (A) UV-vis spectra of OMC, $SiO_2$, and $SiO_2$–OMC; (B) cyclic voltammograms recorded using CPE (a), $SiO_2$/CPE (b), OMC/CPE (c), and $SiO_2$–OMC/CPE (d) using $[Fe(CN)_6]^{3-/4-}$ (5 mmol $L^{-1}$)/PBS (0.1 mol $L^{-1}$) at scan rate of 100 mV $s^{-1}$.

enhancement effect between the $SiO_2$ nanoparticles and OMC materials and the construction of a unique hierarchical and modifiable porous architectures that can make full use of $SiO_2$ the conductive network structure and the high specific surface area of OMC, the $SiO_2$–OMC nanocomposite demonstrates good charge transfer conductance, high specific capacitance, and excellent rate capability.

### Electrochemical sensing of RIB

The electrocatalytic activities of the bare CPE, $SiO_2$/CPE, OMC/CPE, and $SiO_2$–OMC/CPE were investigated for the electro-oxidation of 10 μmol per L RIB in PBS (0.1 mol $L^{-1}$, pH 7.0). As shown in Fig. 5A, the RIB oxidation current at $SiO_2$–OMC/CPE was more pronounced at a potential of 0.71 V. Hybrid $SiO_2$ nanoparticles with OMC have been shown to be efficient for enhancing electron transfer and electrical conductivity. Notably, the oxidation current of RIB on the $SiO_2$–OMC/CPE increased as the pH increased from 5.0 to 7.0, peaking at pH 7.0. It's found that the O–H and $–NH_2$ groups of the RIB are protonated at acidic conditions and the adsorption of RIB might be decreased on the electrode surface, the oxidation current dropped, while RIB exists in its deprotonated form at pH 7.0 and provides hydrogen binding with functional groups of $SiO_2$–OMC causing adsorption of RIB. Moreover, degradation of ribavirin under basic conditions gives a major alkaline degradation product. The rate of acidic hydrolysis was lower when compared with that in alkali.[30] Consequently, pH 7.0 was established as the optimal pH for RIB sensing. Moreover, the linear regression plot was observed for the pH values *vs.* oxidation potential $E_{pa} = 0.049$ pH + 1.317 ($R^2 = 0.992$), indicating an equal number of protons and electrons according to Scheme 1.

The effect of the scan rate on the oxidation current of RIB in PBS (0.1 mol $L^{-1}$, pH 7.0) on the $SiO_2$–OMC/CPE is illustrated in Fig. 5B. A linear relationship between the oxidation current and scan rate was observed, yielding a regression equation of $I$ (μA) $= 0.2074\nu + 10.21$ ($R = 0.992$), as shown in Fig. 5C, suggesting an adsorption-controlled oxidation process.

The adsorption time is a crucial parameter for the detection of RIB on $SiO_2$–OMC/CPE. An increase in the oxidation current of RIB was observed with the increase in adsorption time (Fig. 6A), and the current increased until reaching a plateau at 30 s, indicating saturation of the electrode with adsorbed RIB. Thus, an adsorption time of 30 s was selected as optimal for subsequent tests. Fig. 6B demonstrates the effect of the volume of $SiO_2$–OMC deposited on the CPE in 0.1 mol per L PBS (pH 7.0) for the electro-oxidation of 5 μmol per L RIB. An optimal volume of 5 μL was identified, and smaller volumes resulted in reduced active surface area, whereas larger volumes than 5 μL produced excessively thick $SiO_2$–OMC films.

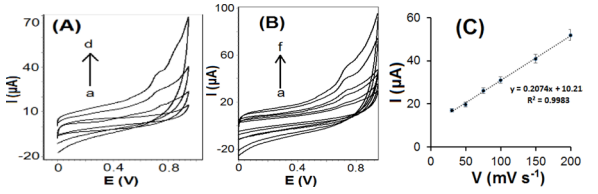


Fig. 5 (A) Cyclic voltammograms of (a) CPE, (b) $SiO_2$/CPE, (c) OMC/CPE, and (d) $SiO_2$–OMC/CPE in the presence of 10 μmol per L RIB. (B) Cyclic voltammograms of 4 μmol per L RIB in 0.1 mol per $L^{-1}$ PBS (pH 7.0) and 0.1 mol per L KCl as supporting electrolyte at the surface of $SiO_2$–OMC/CPE at various scan rates: (a) 30, (b) 50, (c) 75, (d) 100, (e) 150, and (f) 200 mV $s^{-1}$. (C) Plot of peak currents *vs.* scan rates.

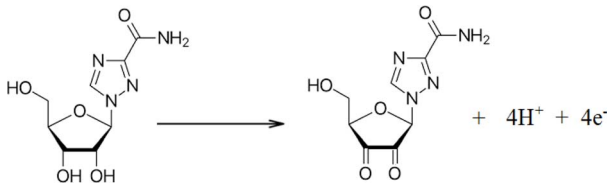


Scheme 1 The oxidation mechanism of RIB.

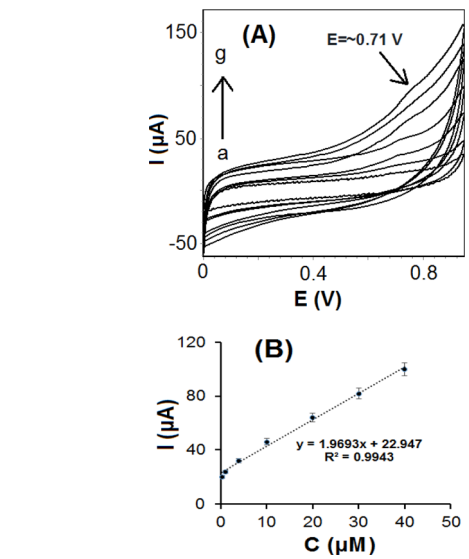


Fig. 6 Effect of (A) adsorption time and (B) volume of $SiO_2$–OMC on oxidation peak current of 5 μmol per L RIB.




Fig. 7 (A) Cyclic voltammograms of $SiO_2$–OMC/CPE in 0.1 mol per L PBS (pH 7.0) in the presence of (a) 0.1, (b) 1, (c) 4, (d) 10, (e) 20, (f) 30, and (g) 40 μmol $L^{-1}$ of RIB. (B) Plot of oxidation peak current *vs.* RIB concentration.

Table 1 Analytical parameters for the determination of RIB using different methods

| Electrode | Method | Linear range (μmol $L^{-1}$) | LOD (μmol $L^{-1}$) | Ref. |
|---|---|---|---|---|
| HMDE | SWAdSV[a] | 0.0001–0.2 | 0.0002 | 18 |
| — | UV-vis | 6.55–81.89 | 0.229 | 5 |
| — | UV-vis | 102.37–342.51 | 0.704 | 5 |
| MIM/Au-PB/GCE | DPV | 0.015–3.50 | 0.003 | 19 |
| APBA/ERGO/GCE | DPV | 0.04–3.07 | — | 17 |
| Pt | Oscillating | 0.15–63 | 0.032 | 20 |
| — | HPLC | 1–64 | 0.100 | 31 |
| — | HPLC | 0.82–20.47 | 0.245 | 32 |
| $SiO_2$–OMC/CPE | CV | 0.1–40 | 0.067 | This work |

[a] Square-wave adsorptive stripping voltammetry.

### Electrochemical performance for the detection of RIB

$SiO_2$–OMC/CPE was further employed for RIB detection in PBS 0.1 mol $L^{-1}$ (pH 7.0). Upon the addition of RIB, the oxidation current was recorded using CV (Fig. 7A). A linear response was obtained for RIB concentrations ranging from 0.1 to 40 μmol $L^{-1}$, with an $R^2$ value of 0.9943, and a regression equation of $I$ (μA) = 22.947 + 1.9693 × [RIB] (μmol $L^{-1}$), as shown in Fig. 7B. The limit of detection (LOD) for RIB was determined to be 0.067 μmol $L^{-1}$. When compared to other methods,[5,17–20,31,32] $SiO_2$–OMC/CPE exhibited a low LOD, as shown in Table 1. Nonetheless, lower LODs have been reported for molecularly imprinted membrane/Prussian blue-gold modified glassy carbon electrodes (3 nmol $L^{-1}$) and HDMEs (2 nmol $L^{-1}$). However, the straightforward fabrication of $SiO_2$–OMC/CPE may offer an advantage for the sensing of clinical samples at the nanomolar level. Moreover, the sensitivity of 1.969 μA $\mu mol^{-1}$ L is particularly noteworthy for RIB sensing in biological fluids.

Next, the reproducibility of $SiO_2$–OMC/CPE fabrication for RIB sensing was investigated. The relative standard deviation (RSD) for the RIB current was determined to be 5.7% at 5 μmol per L RIB across five electrodes. Additionally, the stability of the $SiO_2$–OMC/CPE was assessed, revealing a decrease of 4.2% in RIB current at 5 μmol $L^{-1}$ over 15 days. These results show that OMC is an excellent host for $SiO_2$ nanoparticles, and the $SiO_2$–OMC composite functions as a conductive and stable matrix.

To evaluate the selectivity of the proposed sensor, the sensing of RIB was carried out in the presence of endogenous compounds and other common interfering agents. The interference from cysteine, lysine, glucose, cations ($K^+$, $Na^+$, $Ca^{2+}$, and $Mg^{2+}$), doxorubicin, acetaminophen, uric acid, and ascorbic acid (5 μmol $L^{-1}$ each) was examined for the detection of 5 μmol per L RIB with the $SiO_2$–OMC/CPE in PBS (pH 7.0). The findings (Fig. S1†) indicated only minimal changes in the RIB current in the presence of these interferents, underscoring the high selectivity of the proposed RIB sensor.

### RIB sensing in real samples

The applicability of the proposed method for real sample analysis was validated using CV. Recovery studies to detect RIB in capsules, plasma, and urine were performed to ascertain the efficacy of the $SiO_2$–OMC/CPE. The mean recoveries for RIB ranged from 92.0% to 97.5%, having RSD values of 1.6–4.3%, as determined from standard addition tests (Table 2). This indicates minimal interference from the plasma and urine matrices.

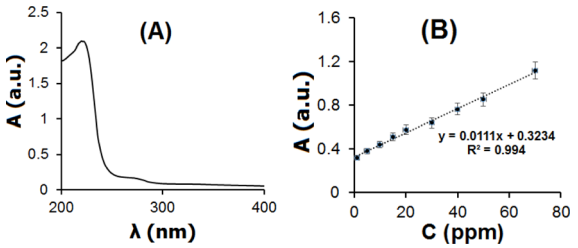


Fig. 8 UV-vis spectrum of RIB 150 ppm in 0.1 mol per L PBS (pH 7.0). (E) Calibration curve for RIB determined by UV-vis spectroscopy.

Table 2 Determination of RIB in real samples at surface of the $SiO_2$–OMC/CPE in 0.1 mol per L PBS solution (pH 7.0)[a]

| Sample | Spiked (μmol $L^{-1}$) | Found (μmol $L^{-1}$) | Mean recovery (%) proposed | Mean recovery (%) UV method | $t_{exp}$ | $F_{exp}$ |
|---|---|---|---|---|---|---|
| Capsule | 5 | 4.7 | 94.0 ± 1.6 | 97.0 ± 3.4 | 1.98 | 5.76 |
| Plasma | — | — | — | — | — | — |
| Plasma | 5 | 4.7 | 96.0 ± 2.1 | — | — | — |
| Plasma | 10 | 9.5 | 97.5 ± 1.9 | — | — | — |
| Urine | — | — | — | — | — | — |
| Urine | 5 | 4.6 | 92.0 ± 3.1 | — | — | — |
| Urine | 10 | 9.7 | 93.5 ± 4.3 | — | — | — |

[a] Theoretical values for $t = 2.31$ and $F = 6.39$ ($p = 0.05$).

Consequently, the $SiO_2$–OMC/CPE was used for the analysis of RIB concentrations in real samples. Furthermore, the results obtained with the $SiO_2$–OMC/CPE sensor were compared with the UV-vis spectroscopy data using *t*-tests and *F*-tests (Table 2). The calculated *t* and *F* values did not exceed the theoretical values at the 95% confidence level, indicating that the precision of the developed sensor is comparable to that of the UV-vis method (Fig. 8).

## Conclusion

A novel and stable $SiO_2$–OMC hybrid was effectively synthesized *via* environmentally friendly process. The results showed sphere-like $SiO_2$ nanoparticles with particle sizes of 21–29 nm decorated onto OMC substrate. A precise and selective sensor, based on the $SiO_2$–OMC hybrid integrated with a CPE, was developed to detect RIB. The $SiO_2$–OMC/CPE sensor could display ultrasensitive and selective detection of RIB at an electro-oxidation potential of 0.71 V within a concentration range of 0.1–40 μM with an LOD of 0.067 μmol $L^{-1}$ and a sensitivity of 1.969 μA μmol $L^{-1}$. The sensor can also be used for the analysis of RIB in capsule, human plasma, and urine and the recoveries were 92.0–97.5%, with RSD values of 1.6–4.3%, suggesting that the proposed sensing methodology might be reliable and effective for monitoring of RIB in clinical specimens.

## Ethical statement

This research with ethical code of IR.IAU.AMOL.REC.1402.141 was approved by Ayatollah Amoli Branch, Islamic Azad University.

## Data availability

The data supporting this article have been included as part of the ESI.†

## Author contributions

All the authors contributed equally in this work.

## Conflicts of interest

The authors declare that they have no conflicts of interest.

## Acknowledgements

The authors are sincerely thankful for the research facilities provided by the Ayatollah Amoli Branch of the Islamic Azad University and the financial support provided by the United Arab Emirates University.

## References

1 G. Taha, L. Ezra and N. Abu-Freha, *Viruses*, 2023, **15**, 1413.
2 P. Mathur, S. Kottilil and E. Wilson, *J. Clin. Transl. Hepatol.*, 2018, **6**, 431.
3 X. Wu, J. Zhang, S. Hu, G. Zhang, H. Lan, J. Peng and H. Liu, *Sci. Total Environ.*, 2022, **850**, 157851.
4 D. Ye, Z. Bao, Y. Yu, Z. Han, Y. Yu, Z. Xu, W. Ma, Y. Yuan, L. Zhang, Y. Xu, T. Ma, S. Liu, X. Gao, G. Yan, Q. Huang, X. Wang, B. Hua, F. Yang, Y. Li and B. Cai, *Toxicology*, 2020, **435**, 152422.
5 N. M. Krishna, *Der Pharma Chem.*, 2018, **10**, 73.
6 A. A. El-Shanawany, A. R. A. Tantawi, A. A. Abdullah, A. S. Al-Hadi, A. A. Suleiman, A. M. Abdulhamid, A. M. Bayoumi, A. H. Ibrahim and M. M. Sebaiy, *Arch. Med. Case Rep. Case Stud.*, 2023, **7**, 158.
7 H. S. Te, G. Randall and D. M. Jensen, *Gastroenterol. Hepatol.*, 2007, **3**, 218.
8 M. Singh and E. de Wit, *Cell Rep. Med.*, 2022, **3**, 100549.
9 M. Kumar, P. Mazumder, S. Mohapatra, A. Kumar Thakur, K. Dhangar, K. Taki, S. Mukherjee, A. Kumar Patel, P. Bhattacharya, P. Mohapatra, J. Rinklebe, M. Kitajima, F. I. Hai, A. Khursheed, H. Furumai, C. Sonne and K. Kuroda, *J. Hazard. Mater.*, 2021, **405**, 124043.
10 A. F. El-Yazbi, Y. Khalifa, M. A. W. Elkhatib and A. F. El-Yazbi, *Microchem. J.*, 2021, **164**, 105964.
11 J. K. Ma, X. C. Huang and S. L. Wei, *J. Sep. Sci.*, 2019, **42**, 3372.
12 I. A. Darwish, H. F. Askal, A. S. Khedr and R. M. Mahmoud, *J. Chromatogr. Sci.*, 2008, **46**, 4.
13 L. Liu, S. Guo, Ch. Che, Q. Su, D. Zhu and X. Hai, *Biomed. Chromatogr.*, 2022, **36**, e5370.
14 Y. L. Wu, R. X. Chen, L. Zhu, Y. Lv, Y. Zhu and J. Zhao, *J. Chromatogr. B*, 2016, **55**, 1012.
15 Y. Lu, Z. Zhang, D. He and Y. Hu, *Anal. Lett.*, 2003, **36**, 1587.
16 M. C. Breadmore, R. Theurillat and W. Thormann, *J. Electroph.*, 2004, **25**, 1615.
17 M. Z. H. Khan, M. Daizy, C. Tarafder and X. Liu, *Sci. Rep.*, 2019, **9**, 19041.
18 A. A. Abdel Gaber, S. A. Ahmed and A. M. Abdel Rahim, *Arab. J. Chem.*, 2017, **10**, S2175.
19 Q. Gao, D. Jin, J. Xu, H. Huang, H. Cheng and H. Xue, *J. Pharm. Biomed. Anal.*, 2023, **230**, 115378.
20 J. Gao, H. Dai, H. Chen, D. Lv, W. Yang, X. Wei and J. Qu, *J. Chil. Chem. Soc.*, 2007, **52**, 1150.
21 X. Du, X. Li, L. Xiong, X. Zhang, F. Kleitz and Sh. Zhang Qiao, *Biomater*, 2016, **91**, 90.
22 Z. Zhu, S. Bai, H. Shang, Q. Tian, J. Sun, X. Wu and J. Liu, *Microporous Mesoporous Mater.*, 2020, **293**, 109768.
23 H. Xu, Y. Pan, H. Kou, Y. Zhu and J. Guo, *J. Alloys Compd.*, 2010, **502**, L6.
24 Y. Gao, Q. Wang, G. Ji, A. Li and J. Niu, *RSC Adv.*, 2021, **11**, 5361.
25 K. Quiroz-Estrada, M. Esparza-Schulz and C. Felipe, *J. Compos. Sci.*, 2022, **6**, 344.
26 A. Walcarius, *Curr. Opin. Electrochem.*, 2018, **10**, 88.
27 H. Bagheri Ladmakhi, S. Fathi, F. Chekin and J. B. Raoof, *Russ. J. Electrochem.*, 2022, **58**, 184.
28 R. Rahimpour, B. Sabeti and F. Chekin, *Russ. J. Electrochem.*, 2021, **57**, 654.

29 E. Vatandost, A. Ghorbani HasanSaraei, F. Chekin, S. Naghizadeh Raeisi and S. A. Shahidi, *Russ. J. Electrochem.*, 2021, **57**, 490.
30 F. Belal, M. K. Sharaf El-Din, M. I. Eid and R. M. El-Gamal, *J. Chromatogr. Sci.*, 2015, **43**, 603.
31 J. V. Svensson, A. Bruchfeld, R. Schvarcz and L. Stahle, *Ther. Drug Monit.*, 2000, **22**, 215.
32 S. Larrat, F. Stanke-Labesque, A. Plages, J. P. Zarski, G. Bessard and C. Souvignet, *Antimicrob. Agents Chemother.*, 2003, **47**, 124.